Journal of Power Sources 192 (2009) 502–514

Contents lists available at ScienceDirect

Journal of Power Sources

journal homepage: www.elsevier.com/locate/jpowsour

Two-dimensional two-phase mass transport model for methanol and water crossover in air-breathing direct methanol fuel cells

Dingding Ye, Xun Zhu, Qiang Liao*, Jun Li, Qian Fu

Institute of Engineering Thermophysics, Chongqing University, Chongqing 400030, China

ARTICLE INFO

Article history:
Received 2 February 2009
Received in revised form 28 February 2009
Accepted 2 March 2009
Available online 14 March 2009

Keywords:
Air-breathing direct methanol fuel cell
Two-phase mass transport model
Methanol crossover
Water crossover

ABSTRACT

A two-dimensional two-phase mass transport model has been developed to predict methanol and water crossover in a semi-passive direct methanol fuel cell with an air-breathing cathode. The mass transport in the catalyst layer and the discontinuity in liquid saturation at the interface between the diffusion layer and catalyst layer are particularly considered. The modeling results agree well with the experimental data of a home-assembled cell. Further studies on the typical two-phase flow and mass transport distributions including species, pressure and liquid saturation in the membrane electrode assembly are investigated. Finally, the methanol crossover flux, the net water transport coefficient, the water crossover flux, and the total water flux at the cathode as well as their contributors are predicted with the present model. The numerical results indicate that diffusion predominates the methanol crossover at low current densities, while electro-osmosis is the dominator at high current densities. The total water flux at the cathode is originated primarily from the water generated by the oxidation reaction of the permeated methanol at low current densities, while the water crossover flux is the main source of the total water flux at high current densities.

© 2009 Elsevier B.V. All rights reserved.

1. Introduction

Direct methanol fuel cells (DMFCs) have been considered as one of the most promising power sources for portable devices due to its high energy density, simple system, fast refueling, low operating temperature, and system simplicity. Fuel cells with neither fuel pumps nor oxidant suppliers are regarded as 'passive', while those with only one reactant by forced convection as 'semi-passive'. In particular, air-breathing DMFCs, which are exposed to atmosphere at cathode side and draw air for its operation entirely through natural convection, have attracted much attention since simpler system eliminates the parasitic power losses caused by auxiliary devices [1–8]. However, the wide application of air-breathing DMFCs is still hindered by many practical problems in materials, fabrication, and operation. Methanol crossover and water crossover are considered as two of the major problems in the DMFCs operation. Methanol crossover will increase the cathode polarization and lower both cell performance and energy conversion efficiency. Water management will cause flooding at the cathode due to difficulties in removing excessive water and further degrade the cell performance. The understanding on the mechanisms and contributors to the methanol crossover and the water crossover will promote the application of the air-breathing DMFCs.

Recently, many experimental investigations have been carried out for passive and air-breathing DMFCs on aspects including optimizing operation conditions [2–8], new fuel delivery systems [9–11], new structures of membrane electrode assembly (MEA) [12,13], effect of methanol crossover [14], and water management [15,16]. However, there are still many difficulties to perform detailed in situ measurement in an operating cell. The numerical simulation provides an available tool to deeply understand the transport interaction and electrochemical phenomena inside the air-breathing DMFC.

Numerous mathematical models have been reported for air-breathing PEMFCs [17–27] and DMFCs [18–34], among which, most considered only single phase model [17–30], while a few adopted two-phase and multi-phase approaches [31–34]. Some papers modeled heat transport in the fuel cells [18,21–27,29,31,33,34], though other papers neglected the thermal effect. Most of the models studied the vertical fuel cells except Xiao and Faghri [34] in which the cell was orientated horizontally. In addition, some of the previous studies treated the catalyst layer as an interface [21,23,27–29,31], others considered the mass transport in the catalyst layer. In these models, the liquid saturation was simulated as continuous at the interface between the diffusion layer and catalyst layer. Actually, a discontinuity in liquid saturation exists at the interface between two kinds of porous media due to continuous capillary pressure and different physical properties according to the classical multi-phase flow theory in porous media. Recently, only Xu et al. [35] and Pasaogullari and Wang [36] accounted for the sudden

* Corresponding author. Tel.: +86 23 6510 2474; fax: +86 23 6510 2474.
E-mail address: lqzx@cqu.edu.cn (Q. Liao).

0378-7753/$ – see front matter © 2009 Elsevier B.V. All rights reserved.
doi:10.1016/j.jpowsour.2009.03.008

Nomenclature

A_v	specific area ($m^2\ m^{-3}$)
C	molar concentration ($mol\ m^{-3}$)
C_0	distribution parameter
D	diffusivity ($m^2\ s^{-1}$)
f	friction factor
F	Faraday constant ($C\ mol^{-1}$)
g	gravitational acceleration ($m\ s^{-2}$)
h_a	height of anode flow channel (m)
h_m	mass transfer coefficient ($m\ s^{-1}$)
I	local current density ($A\ m^{-2}$)
I_{Cell}	cell current density ($A\ m^{-2}$)
I_P	parasitic current density ($A\ m^{-2}$)
j_a	anode current density ($A\ m^{-3}$)
j_c	cathode current density ($A\ m^{-3}$)
j_0	exchange current density ($A\ m^{-2}$)
k_c	condensation rate (s^{-1})
k_e	evaporation rate ($atm^{-1}\ s^{-1}$)
k_r	relative permeability
K	permeability of porous media (m^2)
l	length of flow channel (m)
m	mass flux ($kg\ m^{-2}\ s^{-1}$)
$\dot{m}$	source term in mass conservation equation ($kg\ m^{-3}\ s^{-1}$)
M	molecular weight ($kg\ mol^{-1}$)
n_d	electro-osmotic drag coefficient
N	mol flux ($mol\ m^{-2}\ s^{-1}$), or Nafion
p	pressure (Pa)
p_c	capillary pressure (Pa)
p_g	gas phase pressure (Pa)
p_l	liquid phase pressure (Pa)
R	gas constant ($J\ mol^{-1}\ K^{-1}$)
RH	relative humidity
$\dot{R}$	source term in species conservation equation ($mol\ m^{-3}\ s^{-1}$)
$R_{contact}$	ohmic contact resistance ($\Omega\ m^2$)
$\dot{R}_w$	interfacial transfer rate of water between liquid and vapor ($mol\ m^{-3}\ s^{-1}$)
s	liquid saturation
Sc	Schmidt number
Sh	Sherwood number
T	temperature (K)
$\mathbf{u}$	superficial velocity vector ($m\ s^{-1}$)
u	phase velocity ($m\ s^{-1}$)
u_{gj}	drift velocity ($m\ s^{-1}$)
V_{Cell}	cell voltage (V)
V_0	thermodynamic equilibrium potential (V)
w_a	width of anode flow channel (m)
x	coordinate (mm), or mole fraction in liquid solution
y	coordinate (mm), or mole fraction in gas mixture

Greek letters

α	void fraction in flow channel
α_a	transfer coefficient of anode
α_c	transfer coefficient of cathode
α_w	net water transport coefficient
γ	reaction order
δ	thickness of porous layer (m)
ε	porosity of porous layer
η	overpotential (V)
θ_c	contact angle (°)
κ	ionic conductivity of membrane ($\Omega^{-1}\ m^{-1}$)
μ	viscosity ($kg\ m^{-1}\ s^{-1}$)
ρ	density ($kg\ m^{-3}$)
σ	surface tension ($N\ m^{-1}$)

Superscripts

acl	anode catalyst layer
adl	anode diffusion layer
afc	anode flow channel
amb	ambient
ccl	cathode catalyst layer
cdl	cathode diffusion layer
eff	effective value
mem	membrane
ref	reference value
sat	saturated value
—	average value

Subscripts

a	anode
c	cathode
Cell	cell
g	gas phase
l	liquid phase
MeOH	methanol
O_2	oxygen
v	vapor
w	liquid water

change of liquid saturation in their models on the water transport in DMFCs and PEMFCs, respectively.

In the present study, a two-dimensional two-phase mass transport model is developed to predict methanol and water crossover in a semi-passive direct methanol fuel cell with an air-breathing cathode. In addition to the mass transport in the catalyst layer, the discontinuity in liquid saturation at the interface between the diffusion layer and catalyst layer is also taken into account. The drift–flux model is adopted to describe the two-phase flow in the anode channels. The mass transport in the anode porous region is modeled by the classical multi-phase flow in porous media theory, in which various phases are regarded as distinct fluids with individual thermodynamic and transport properties and with different flow velocities. However, the mass transport in the cathode is formulated based on the unsaturated flow theory (UFT), in which the gas pressure is assumed to be constant across the entire porous region. The predicted results are validated with experimental data by a home-assembled cell. Typical two-phase flow and mass transport distributions at the anode and the cathode, methanol crossover flux, net water transport coefficient, water crossover flux, as well as the total water flux at the cathode and their contributors are investigated with this model.

2. Numerical model

A vertical air-breathing DMFC simulated in the present study is shown in Fig. 1 and methanol aqueous solution is fed by a pump in the direction as marked. The computational domain consists of all six parts of the air-breathing DMFC, including anode flow channel (AFC), anode diffusion layer (ADL), anode catalyst layer (ACL), membrane (MEM), cathode catalyst layer (CCL) and cathode diffusion layer (CDL). At the anode, methanol aqueous solution is fed into the AFC and then transfers through the ADL into the ACL, where one part of methanol is oxidized to generate CO_2 gas, while another part permeates through the MEM into the cathode. The produced CO_2 gas goes through the ADL, emerges into the AFC in bubbles and

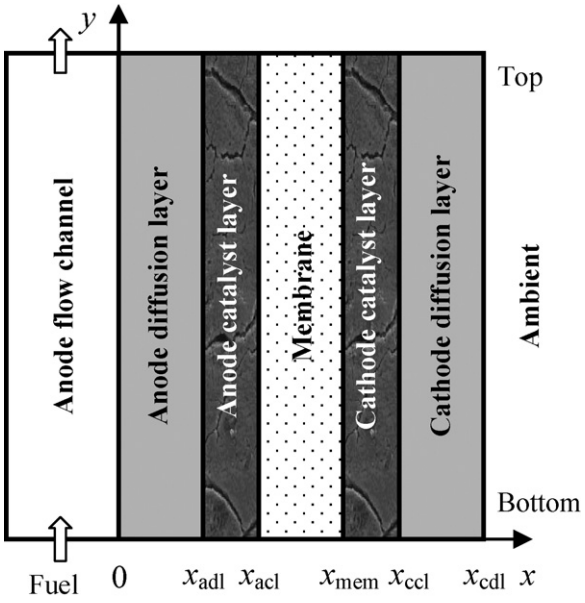

Fig. 1. Schematic of a vertical air-breathing DMFC.

then removes with flowing methanol solution in the AFC. At the cathode, the oxygen from the ambient air diffuses through the CDL into the CCL, where it reduces with the electrons from the circuit and the protons from the anode to form water. The produced water is expelled through the CDL by the capillary pressure along with evaporation.

Several coupled complex physicochemical processes occur simultaneously in such an operation air-breathing DMFC, which makes it quite difficult to simulate comprehensively. For the numerical realization of the present model, the following assumptions, which are reasonable and acceptable to some extent based on the practical operation DMFC, are used:

(1) The cell operates under steady-state and isothermal conditions.
(2) Thermal physical properties of fluids are considered as constant.
(3) The fluid flow in the AFC is one-dimensional, i.e., the flow along *x*-direction is ignored.
(4) Considering the thicknesses of ADL, ACL, MEM, CCL and CDL are much smaller than their sizes along *y*-direction, the flow and mass transport along *y*-direction are neglected.
(5) The ADL, ACL, MEM, CCL and CDL are isotropic porous media.
(6) At the anode, the gas fluid is considered only from the produced CO_2 gas, i.e., the evaporation of methanol and water is ignored.
(7) The methanol permeated from the anode is oxidized completely at the interface between the MEM and CCL.
(8) The gas pressure at the cathode is a constant since the cathode is exposed to the ambient.
(9) At the cathode, the gases are transferred from the ambient to the CDL by natural convection.

2.1. Anode flow channel

Visualization experiments for DMFCs [37,38] showed that the two-phase flow pattern in AFC varied from homogeneous to slug flow depending on the cell operating conditions. The amount of gas CO_2 in the AFC increased with increasing current density, and the gas bubbles or slugs were removed periodically by the solution in the channel. Thus it can be seen that a complicated two-phase flow happens in the AFC of a practical operating DMFC. In the present work, a drift–flux model, which is firstly used for a DMFC by Wang and Wang [39], is adopted to describe gas–liquid two-phase flow in the anode channel. Details are presented below.

The continuity equations for two phases in the AFC can be given by:

$$\nabla[\rho_l \bar{u}_l(1-\alpha)] = -\frac{m_l^{afc}}{h_a} \text{ (liquid phase)}, \quad (1)$$

$$\nabla(\rho_g \bar{u}_g \alpha) = -\frac{m_g^{afc}}{h_a} \text{ (gas phase)}, \quad (2)$$

where the subscripts 'l' and 'g' refer to the liquid phase and the gas phase, respectively, $\bar{u}$ represents the average velocity across the flow channel, α is the cross-sectional mean gas void fraction, m^{afc} denotes the mass flux at the interface between the AFC and ADL, and h_a is the height of the AFC cross-section.

The momentum equation for the vertical anode channel can be written as:

$$\nabla[\rho_l \bar{u}_l \bar{u}_l(1-\alpha)] + \nabla(\rho_g \bar{u}_g \bar{u}_g \alpha) = -\nabla p - 2\rho_m \frac{f_m}{D_h} \bar{u}_m \bar{u}_m - \rho_m g, \quad (3)$$

where p is the liquid pressure in the AFC, ρ_m the two-phase volume-averaged density $\rho_m = \rho_l(1-\alpha) + \rho_g\alpha$, f_m the friction factor, D_h the hydraulic diameter of the AFC, and $\bar{u}_m$ represents the average velocity of the two-phase mixture and is given as:

$$\bar{u}_m = \alpha \bar{u}_g + (1-\alpha)\bar{u}_l. \quad (4)$$

According to the drift–flux model, the relationship between the velocities of liquid and gas phases can be described by the following equation:

$$\bar{u}_g = C_0[\alpha \bar{u}_g + (1-\alpha)\bar{u}_l] + u_{gj}, \quad (5)$$

where C_0 represents the distribution parameter and u_{gj} is the drift velocity. The distribution parameter and the drift velocity for slug flow through a rectangular channel are given by:

$$C_0 = 1.35 - 0.35\sqrt{\frac{\rho_g}{\rho_l}}, \quad (6)$$

$$u_{gj} = \left(0.23 + 0.13\frac{h_a}{w_a}\right)\sqrt{\frac{(\rho_l - \rho_g)g w_a}{\rho_l}}, \quad (7)$$

where w_a is the width of the AFC.

The species balance equation for methanol in the AFC can be written as:

$$\nabla[(1-\alpha)\bar{u}_l \bar{C}_{MeOH}] = -\frac{N_{MeOH}^{afc}}{h_a}, \quad (8)$$

where $\bar{C}_{MeOH}$ is the cross-sectional average methanol concentration and N_{MeOH}^{afc} represents the mole flux of methanol at the interface between the AFC and ADL.

2.2. Anode porous region

The anode porous region consists of the ADL and ACL. The ADL is composed of inactive carbon and no electrochemical reaction occurs within this region. The ACL provides catalytic sites for methanol oxidation. The transport behavior in the anode porous region, where the transport of methanol solution is driven by convection and diffusion, is modeled based on the classical two-phase flow in porous media. The mass conservation equations for the two phases in the anode porous region are given by:

$$\nabla(\rho_l \mathbf{u}_l) = \dot{m}_{l,a} \text{ (liquid phase)}, \quad (9)$$

$$\nabla(\rho_g \mathbf{u}_g) = \dot{m}_{g,a} \text{ (gas phase)}, \quad (10)$$

where $\mathbf{u}$ is the superficial velocity vector in the porous media and $\dot{m}$ represents the mass source (see Table 1), subscript 'a' refers to the anode.

Table 1
Correlations used in this model.

Parameters	Expressions
Relative permeability	$k_{rl} = s^3$ liquid $k_{rg} = (1-s)^3$ gas
Effective diffusion coefficients of species	$D_i^{eff} = D_i \varepsilon^{1.5} s^{1.5}$ i : O_2, vapor CDL/CCL
	$D_{MeOH}^{eff} = \begin{cases} D_{MeOH,l}\varepsilon^{1.5}s^{1.5} & \text{ADL} \\ \dfrac{\varepsilon+\varepsilon_N}{[\varepsilon/(D_{MeOH,l}\varepsilon^{1.5}s^{1.5})+\varepsilon_N/(D_{MeOH,N}\varepsilon_N{}^{1.5})]} & \text{ACL} \\ D_{MeOH,N}\varepsilon^{1.5} & \text{MEM} \end{cases}$
General generation rate of mass in liquid phase	$\dot{m}_{l,a} = \begin{cases} 0 & \text{ADL} \\ -M_w\dfrac{j_a}{6F} - M_{MeOH}\dfrac{j_a}{6F} & \text{ACL} \end{cases}$
	$\dot{m}_{l,c} = \begin{cases} -M_w\dot{R}_w & \text{CDL} \\ M_w\left(\dfrac{j_c}{2F} - \dfrac{I_P}{6F\delta_{ccl}}\right) - M_w\dot{R}_w & \text{CCL} \end{cases}$
General generation rate of mass gas phase	$\dot{m}_{g,a} = \begin{cases} 0 & \text{ADL} \\ M_{CO_2}\dfrac{j_a}{6F} & \text{ACL} \end{cases}$
Mole generation rate of species	$\dot{R}_{MeOH} = \begin{cases} 0 & \text{ADL} \\ -\dfrac{j_a}{6F} & \text{ACL} \end{cases}$
	$\dot{R}_{O_2} = \begin{cases} 0 & \text{CDL} \\ -\dfrac{j_c}{4F} & \text{CCL} \end{cases}$
The saturation pressure of water vapor	$\log_{10} p_v^{sat} = -2.1794 + 0.02953(T-273) - 9.1837\times10^{-5}(T-273)^2 + 1.4454\times10^{-7}(T-273)^3$ atm
Interfacial transfer rate of water between liquid and vapor	$\dot{R}_w = \begin{cases} k_e\dfrac{\varepsilon s\rho_l}{M_w}(y_v p_g - p_v^{sat}) & y_v p_g < p_v^{sat} \\ k_c\dfrac{\varepsilon(1-s)y_v}{RT}(y_v p_g - p_v^{sat}) & y_v p_g > p_v^{sat} \end{cases}$

The momentum equations in the anode porous region are described by Darcy's law as:

$$\mathbf{u}_l = -K\frac{k_{rl}}{\mu_l}\nabla p_{l,a} \text{ (liquid phase)}, \tag{11}$$

$$\mathbf{u}_g = -K\frac{k_{rg}}{\mu_g}\nabla p_{g,a} \text{ (gas phase)}, \tag{12}$$

where K, k_{rl} and k_{rg} denote the absolute permeability of porous media, the relative permeability of liquid and gas (see Table 1), respectively, μ_l and μ_g are the viscosity of liquid and gas. The gas pressure, p_g, and the liquid pressure, p_l, relate to the capillary pressure, p_c, which is defined by:

$$p_c = p_g - p_l = \sigma\cos\theta_c\left(\frac{\varepsilon}{K}\right)^{1/2}J(s), \tag{13}$$

where σ is the surface tension of methanol solution, θ_c the contact angle, ε the porosity of porous media, and $J(s)$ stands for the Levertte function and can be given by [40]:

$$J(s) = \begin{cases} 1.417(1-s) - 2.120(1-s)^2 + 1.263(1-s)^3 & 0 < \theta_c < 90^\circ \\ 1.417s - 2.120s^2 + 1.263s^3 & 90^\circ < \theta_c < 180^\circ \end{cases} \tag{14}$$

The wettability of the ADL and ACL is set to be hydrophobic in the present study, hence the contact angles larger than 90° (see Table 4).

The species conservation of methanol in the anode porous region can be expressed as:

$$\nabla(\mathbf{u}_l C_{MeOH}) + \nabla(-D_{MeOH}^{eff}\nabla C_{MeOH}) = \dot{R}_{MeOH}, \tag{15}$$

where C_{MeOH} and D_{MeOH}^{eff} represent the methanol concentration and the effective diffusion coefficient of methanol (see Table 1), respectively. The first term on the left-hand side of Eq. (15) denotes the convection term of methanol transport, while the second term describes the diffusive transport, and the source term $\dot{R}_{MeOH}$ stands for the mole generation rate of methanol due to the electrochemical reaction (see Table 1).

2.3. Membrane

Only mass transport of the liquid methanol and water across the MEM is taken into account due to the impermeability of the proton exchange membrane for gases. It is noted that the methanol transport through the membrane is driven by diffusion, electro-osmosis, and hydraulic pressure gradient across the membrane. Thus, the flux of methanol crossover can be given by:

$$N_{MeOH}^{mem} = -D_{MeOH}^{mem,eff}\nabla C_{MeOH}^{mem} + n_{d,MeOH}\frac{I}{F} - C_{MeOH}^{mem}\frac{K(p_{l,c}-p_{l,a})}{\mu_l\delta_{mem}}, \tag{16}$$

where $D_{MeOH}^{mem,eff}$ is the effective diffusivity of methanol in the membrane, δ_{mem} the thickness of the membrane, $n_{d,MeOH}$ denotes the electro-osmotic drag coefficient of methanol, $n_{d,MeOH} = n_{d,w}x_{MeOH}$, $n_{d,w}$ the electro-osmotic drag coefficient of water, and x_{MeOH} the mole fraction of methanol solution.

The methanol flux is uniform through the membrane due to no electrochemical reaction in the MEM, i.e.,

$$\nabla N_{MeOH}^{mem} = 0. \tag{17}$$

Furthermore, the transport mechanism of liquid water through the membrane is similar to that of methanol. However, the water concentration difference across the membrane is considerably small leading to the water diffusion being neglected. Therefore, the water flux is expressed as follows:

$$N_w^{mem} = n_{d,w}\frac{I}{F} - \frac{\rho_l}{M_w}\frac{K(p_{l,c}-p_{l,a})}{\mu_l\delta_{mem}}. \tag{18}$$

2.4. Cathode porous region

The cathode porous region consists of the CDL and CCL. Similarly, the CDL is composed of inactive carbon and no electrochemical reaction occurs within this region, while the CCL provides catalytic sites for oxygen reduction. The wettability of the CDL and CCL is also set to be hydrophobic. The two-phase flow in the cathode porous

region is modeled with the unsaturated flow theory. Since gas pressure at the cathode is assumed to be a constant, the transport of gases in the cathode porous region is dominated by diffusion. The liquid water generated in the CCL removes through the CDL by the capillary pressure coupled with evaporation.

The mass conservation of the liquid in the cathode porous region can be modeled by:

$$\nabla(\rho_w \mathbf{u}_{l,c}) = \dot{m}_{l,c}, \tag{19}$$

where subscript 'w' refers to liquid water and 'c' the cathode.

The momentum equation of the liquid can be obtained from Darcy's law:

$$\mathbf{u}_{l,c} = -K\frac{k_{rl,c}}{\mu_w}\nabla p_{l,c}, \tag{20}$$

where μ_w is the viscosity of the liquid water. With the aid of the definition of the capillary pressure shown in Eq. (13) and the assumption of the constant gas pressure across the cathode porous region, Eq. (20) can be rewritten as:

$$\mathbf{u}_{l,c} = K\frac{k_{rl,c}}{\mu_w}\sigma_w \cos\theta_c\left(\frac{\varepsilon}{K}\right)^{1/2}\nabla J(s). \tag{21}$$

The mass transport of the gases in the cathode porous region can be modeled by:

$$\nabla(-D_v^{eff}\nabla C_v) = \dot{R}_w, \tag{22}$$

$$\nabla(-D_{O_2}^{eff}\nabla C_{O_2}) = \dot{R}_{O_2}, \tag{23}$$

where D_v^{eff} and $D_{O_2}^{eff}$ represent the effective diffusivity of vapor and oxygen, respectively, $\dot{R}_w$ is the interfacial transfer rate of water between liquid and vapor, and $\dot{R}_{O_2}$ the mole generation rate of oxygen (see Table 1).

2.5. Electrochemical kinetics

At the anode, a simplified Tafel equation is employed to model the kinetics of methanol oxidation reaction (MOR):

$$j_a = A_{v,a} j_{0,MeOH}^{ref}\left(\frac{C_{MeOH}^{acl}}{C_{MeOH}^{ref}}\right)^{\gamma}\exp\left(\frac{\alpha_a F}{RT}\eta_a\right), \tag{24}$$

where $A_{v,a}$ represents the specific area of the anode, $j_{0,MeOH}^{ref}$ is the reference exchange current density of the anode, C_{MeOH}^{ref} the reference methanol concentration, and γ the reaction order and given by:

$$\gamma = \begin{cases} 0 & C_{MeOH}^{acl} > C_{MeOH}^{ref} \\ 1 & C_{MeOH}^{acl} \le C_{MeOH}^{ref} \end{cases}, \tag{25}$$

which means the methanol oxidation is a zero-order reaction when methanol concentration is higher than a reference value, otherwise, a first-order reaction is considered in this model.

At the cathode, the first-order Tafel kinetics is used to describe the oxygen reduction reaction (ORR):

$$j_c = (1-s)A_{v,c} j_{0,O_2}^{ref}\left(\frac{C_{O_2}^{ccl}}{C_{O_2}^{ref}}\right)\exp\left(\frac{\alpha_c F}{RT}\eta_c\right), \tag{26}$$

where $A_{v,c}$ represents the specific area of the cathode, j_{0,O_2}^{ref} the reference exchange current density of oxygen, and $C_{O_2}^{ref}$ the reference oxygen concentration.

2.6. Boundary conditions

At the inlet of the AFC, all variables can be given according to the fuel supply conditions:

$$\bar{u}_l^{afc} = \frac{Q_{l,a}^{in}}{nh_a w_a}, \quad \bar{C}_{MeOH}^{afc} = C_{MeOH}^{in}, \quad p_l = p_{l,a}^{in}, \quad (1-\alpha) = \bar{s} = s_{l,a}^{in}. \tag{27}$$

The continuity and mass/species flux balance conditions are employed at each interface. Detailed description of the boundary conditions for each interface is given in Table 2. It should be noted that the capillary pressure is continuous at $x = x_{adl}$ and $x = x_{ccl}$, while different properties of the porous media result in a discontinuity of the liquid saturation at these interfaces.

It is difficult to determine the liquid saturation at the outer surface of the CDL in the air-breathing DMFC. Actually, it changes with the operation condition and the current density. For simplification, a constant value is given to the liquid saturation at the CDL surface in present model, i.e., $s_{l,c}^0 = 0.05$ [31].

Table 2
Boundary conditions.

Interface	Species	Flux	Pressure	Liquid saturation
$x=0$	$\bar{C}_{MeOH}^{afc} = C_{MeOH}^{adl}$	$N_{MeOH}^{afc} = N_{MeOH}^{adl}$ $m_l^{afc} = m_{MeOH}^{adl}$ $m_g^{afc} = m_{MeOH}^{adl}$	$p_l^{afc} = p_l^{adl}$	$(1-\alpha) = \bar{s}_l^{afc} = s_l^{adl}$
$x=x_{adl}$	$C_{MeOH}^{adl} = C_{MeOH}^{acl}$	$N_{MeOH}^{adl} = N_{MeOH}^{acl}$ $m_l^{adl} = m_l^{acl}$ $m_g^{adl} = m_g^{acl}$	$p_l^{adl} = p_l^{acl}$ $p_c^{adl} = p_c^{acl}$	$\cos\theta_{adl}\left(\frac{\varepsilon_{adl}}{K_{adl}}\right)^{1/2}J(s_l^{adl}) = \cos\theta_{acl}\left(\frac{\varepsilon_{acl}}{K_{acl}}\right)^{1/2}J(s_l^{acl})$
$x=x_{acl}$	$C_{MeOH}^{acl} = C_{MeOH}^{mem}$	$N_{MeOH}^{acl} = N_{MeOH}^{mem}$ $m_l^{acl} = m_l^{mem}$, $m_g^{acl} = 0$	$\nabla p_l^{acl} = -\frac{\mu_l/\rho_l}{Kk_{rl}}(m_l^{acl})$ $\nabla p_g^{acl} = 0$	
$x=x_{mem}$	$C_{MeOH}^{mem} = C_{MeOH}^{ccl} = 0$	$N_{MeOH}^{mem} = N_{MeOH}^{ccl}$ $N_{O_2}^{ccl} = 0$, $N_v^{ccl} = 0$, $m_l^{mem} = m_l^{ccl}$, $m_g^{ccl} = 0$	$\nabla p_l^{ccl} = -\frac{\mu_l/\rho_l}{Kk_{rl}}(m_l^{ccl})$ $\nabla p_g^{ccl} = 0$	
$x=x_{ccl}$	$C_{O_2}^{ccl} = C_{O_2}^{cdl}$ $C_v^{ccl} = C_v^{cdl}$	$N_{O_2}^{ccl} = N_{O_2}^{cdl}$ $N_v^{ccl} = N_v^{cdl}$ $m_l^{ccl} = m_l^{cdl}$ $m_g^{ccl} = m_g^{cdl}$	$p_l^{cdl} = p_l^{ccl}$ $p_c^{cdl} = p_c^{ccl}$	$\cos\theta_{ccl}\left(\frac{\varepsilon_{ccl}}{K_{ccl}}\right)^{1/2}J(s_l^{ccl}) = \cos\theta_{cdl}\left(\frac{\varepsilon_{cdl}}{K_{cdl}}\right)^{1/2}J(s_l^{cdl})$
$x=x_{cdl}$		$N_{O_2}^{cdl} = h_{O_2}(C_{O_2}^{amb} - C_{O_2}^{cdl})$ $N_v^{cdl} = h_v(C_v^{amb} - C_v^{cdl})$	$p_g^{cdl} = p_{g,c}$	$s_l^{cdl} = s_{l,c}^0$

The gases transfer between the CDL and the ambient air by natural convection. Therefore the mass transfer coefficient at the interface of $x = x_{cdl}$ can be obtained from the natural convection correlation on a vertical surface [17]:

$$Sh = \frac{h_m L}{D} = 0.68 + \frac{0.67 Ra_M^{1/4}}{[1 + (0.492/Sc)^{9/16}]^{4/9}}, \quad (28)$$

where Sh is the Sherwood number, Sc the Schmidt number ($Sc = \nu/D$), and Ra_M the Rayleigh number ($Ra_M = (\gamma g(w_w - w_\infty)L^3)/\nu D$).

2.7. Cell performance

The electrochemical reaction rate varies with the reactant concentration along both x-direction and y-direction. As a result, the local current density and the average cell current density can be given by:

$$I = \int_{acl} j_a dx, \quad (29)$$

and

$$I_{Cell} = \frac{\iint_{acl} j_a dx dy}{l}. \quad (30)$$

Furthermore, the parasitic current density caused by the methanol crossover is calculated by:

$$I_P = 6FN_{MeOH}^{mem}. \quad (31)$$

The current balance in the cell is described as:

$$I + I_P = \int_{ccl} j_c dx. \quad (32)$$

Thus, the cell voltage is expressed as:

$$V_{Cell} = V_0 - \eta_a - \eta_c - I_{Cell}\left(R_{contact} + \frac{\delta_{mem}}{\kappa}\right), \quad (33)$$

where V_0 is the thermodynamic equilibrium potential of a DMFC, $R_{contact}$ the contact resistance of the fuel cell, and κ denotes the proton conductivity of the membrane.

2.8. Numerical method

The above governing equations are iteratively solved by the finite volume method using a self-written code in FORTRAN language based on the tridiagonal matrix algorithm (TDMA) until the convergence criterions are satisfied. The operating parameters and the physicochemical properties used in the calculations are listed in Tables 3 and 4, respectively. For a given anode overpotential η_a, the methanol concentration distribution can be obtained using Eqs. (1)–(18). Then the average cell current density, I_{Cell}, and the parasitic current density, I_P, can be determined from Eqs. (30) and (31). The cathode overpotential, η_c, can be calculated from Eq. (32) based on the oxygen concentration distribution and the cathode current density, j_c, obtained from Eqs. (19)–(23) and (26). Finally, the anode and the cathode overpotentials are substituted into Eq. (33) to calculate the cell voltage V_{Cell}. Such a computation process is repeated until the polarization curve is obtained.

3. Results and discussion

3.1. Model validation

An air-breathing DMFC with an active area of $2.1 \times 2.1\ cm^2$ was fabricated and tested to validate the above model. A carbon paper (Toray, TGP-H-090) with 15% polytetrafluoroethylene (PTFE) wetproofing treatment was used as the backing support layer in the anode and the cathode. The anode catalyst loading was 3.0 mg cm^{-2} with Pt–Ru black (1:1, a/o), while the cathode catalyst loading was 5.0 mg cm^{-2} using Pt black. The membrane electrode assembly was formed by hot pressing a pretreated Nafion 117 membrane between the two electrodes at 135 °C and 10 MPa for 3 min. The prepared MEA was sandwiched between two stainless steel plates, in which the straight flow channels were fabricated. The methanol solution was fed into the anode by a peristaltic pump. The cathode electrode was exposed to atmosphere and oxygen was drawn directly from the ambient air by natural convection. The voltage–current curves were recorded by an Arbin Fuel Cell Test system (FCTs-1000).

Table 3
Operating parameters.

Parameter	Symbol	Value	Unit
Anode flow channel length	l	2.1×10^{-2}	m
Anode flow channel height	h_a	2.0×10^{-3}	m
Anode flow channel width	w_a	1.8×10^{-3}	m
Anode flow channel number	n	7	–
Thickness of ADL and CDL	l_{dl}	2.6×10^{-4}	m
Thickness of ACL and CCL	l_{cl}	2.0×10^{-5}	m
Thickness of MEM	l_m	1.8×10^{-4}	m
Operating temperature	T	298.0	K
Anode inlet pressure	$p_{l,a}^{in}$	1.013×10^5	Pa
Cathode gas pressure	$p_{g,c}$	1.013×10^5	Pa
Total anode flow rate	$Q_{l,a}^{in}$	1.0	ml min^{-1}
Inlet methanol concentration at anode	C_{MeOH}^{in}	4000	mol m^{-3}
Relative humidity of air	RH_{air}	60%	–
Contact resistance	$R_{contact}$	8.0×10^{-5}	$\Omega\,m^2$

The modeling results of the cell polarization curve are compared with the experimental data in Fig. 2. It can be seen that the numerical results agree well with the experimental data within a wide current density range. The slight disagreement at low current densities might be resulted from the Tafel kinetics employed in this model. Based on the good agreement with the data, the further studies on species distributions, pressure, liquid saturation, as well as methanol and water crossover are performed as follows with the help of the above model. Unless specified otherwise, the modeling results on the distributions are obtained with 4 M methanol concentration and at the current density of 720.78 A m^{-2} (η_a = 0.385 V).

3.2. Reactants concentration distributions

It is known that methanol transfers from the AFC through the ADL to the ACL at the anode and permeates through the MEM to the cathode. Fig. 3 shows the methanol concentration distribution

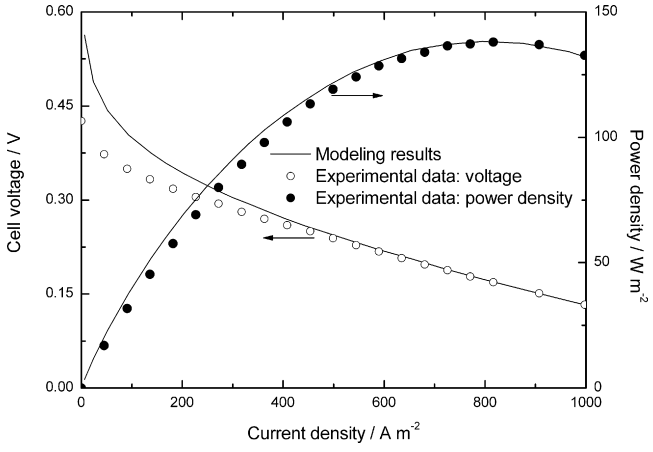

Fig. 2. Comparison of the modeling results with the experimental data.

Table 4
Physicochemical properties.

Parameter	Symbol	Value	Unit	Ref.
Porosity of ADL and CDL	ε_{adl}, ε_{cdl}	0.7	–	[41]
Porosity of ACL and CCL	ε_{acl}, ε_{ccl}	0.4	–	[18]
Porosity of MEM	ε_{m}	0.3	–	[41]
Permeability of ADL and CDL	K_{adl}, K_{cdl}	1.0×10^{-12}	m^2	[41]
Permeability of ACL and CCL	K_{acl}, K_{ccl}	1.5×10^{-14}	m^2	[35]
Permeability of MEM	K_{m}	2.0×10^{-18}	m^2	[41]
Nafion volume fraction of ACL and CCL	ε_{N}	0.3	–	[35]
Diffusivity of MeOH in water	$D_{MeOH,l}$	$10^{-5.4163 - 999.778/T}$	$m^2\ s^{-1}$	[39]
Diffusivity of MeOH in Nafion	$D_{MeOH,N}$	$4.9 \times 10^{-10} e^{[2436(1/333 - 1/T)]}$	$m^2\ s^{-1}$	[41]
Diffusivity of oxygen	D_{O_2}	$0.1775 \times 10^{-4} \left(\frac{T}{273.15}\right)^{1.823}$	$m^2\ s^{-1}$	[39]
Diffusivity of water vapor	D_{v}	$0.256 \times 10^{-4} \left(\frac{T}{273.15}\right)^{2.334}$	$m^2\ s^{-1}$	[39]
Electro-osmotic drag coefficient of water	$n_{d,w}$	$2.9e^{[1029(1/333 - 1/T)]}$	–	[29]
Electro-osmotic drag coefficient of methanol	$n_{d,MeOH}$	$n_{d,w} x_{MeOH}$	–	[39]
Surface tension of methanol solution	σ	5.146×10^{-2}	$N\ m^{-1}$	
Density of methanol solution	ρ_{l}	962.76	$kg\ m^{-3}$	
Dynamic viscosity of methanol solution	μ_{l}	8.592×10^{-4}	$kg\ m^{-1}\ s^{-1}$	
Viscosity of air	μ_{g}	1.5535×10^{-5}	$kg\ m^{-1}\ s^{-1}$	
Evaporation rate constant	k_{e}	1	$1\ atm^{-1}\ s^{-1}$	[29]
Condensation rate constant	k_{c}	100	$1\ s^{-1}$	[29]
Reference concentration of methanol	C^{ref}_{MeOH}	100	$mol\ m^{-3}$	[39]
Reference concentration of oxygen	$C^{ref}_{O_2}$	8.58	$mol\ m^{-3}$	[29]
Transfer coefficient of anode	α_{a}	0.5	–	[41]
Transfer coefficient of cathode	α_{c}	0.7	–	
Reference exchange current density times specific area at anode	$A_{v,a} j^{ref}_{0,MeOH}$	2.0×10^{4}	$A\ m^{-3}$	
Reference exchange current density times specific area at cathode	$A_{v,c} j^{ref}_{0,O_2}$	$\frac{0.04222e[73200/R(1/353 - 1/T)]}{l_{cl}}$	$A\ m^{-3}$	[32]

in the anode porous region and MEM. Apparently, the methanol concentration decreases linearly across the ADL, while a non-linear drop is observed across the ACL due to the methanol oxidation reaction there. Finally, it goes down to zero at $x = x_{mem}$ since the permeated methanol through the MEM is assumed to be completely oxidized at the cathode side. The methanol mass flux is constant in the ADL and MEM due to no electrochemical reaction, but decreases in the ACL as a result of methanol consumption. In addition, a slight decrease in the methanol concentration along the anode flow channel could be also attributed to the methanol consumption.

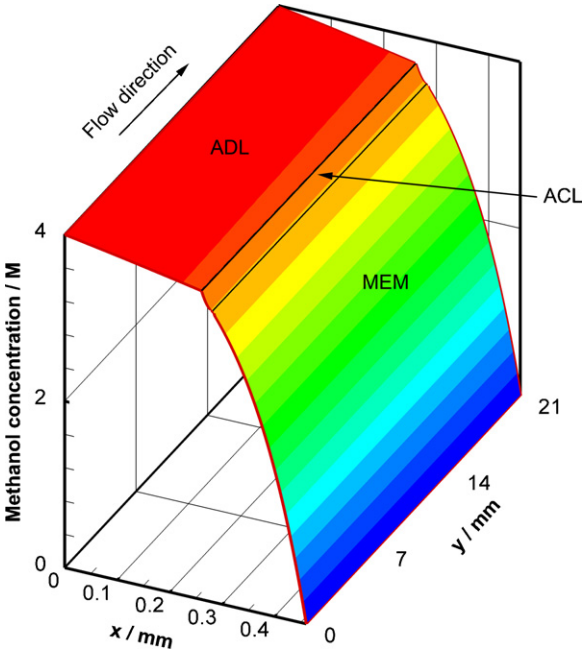

Fig. 3. The distribution of methanol concentration in the anode porous region and MEM.

Oxygen supplied by the ambient air diffuses through the CDL to the CCL at the cathode. The oxygen concentration distribution in the cathode porous region is also predicted as shown in Fig. 4. It can be seen that the oxygen concentration decreases from the CDL to the CCL, and then goes down non-linearly across the CCL. Similarly, the oxygen mass flux is constant in the CDL, while it decreases in the CCL due to the oxygen reduction reaction. In contrast to the anode, a slight increase in the oxygen concentration along the y-direction is observed. And the main reason for this slight increase may be considered as oxidation of the permeated methanol by oxygen in the CCL. The decrease in the methanol concentration along the y-direction at the anode results in a decrease in the methanol crossover flux leading to lower oxygen consumption rate at the cathode. Thus, the oxygen concentration at the CDL surface increases according to the boundary condition at $x = x_{cdl}$.

3.3. Pressure distribution

The distribution of liquid pressure in the anode porous region is shown in Fig. 5 where the liquid pressure near the interface $x = x_{adl}$ is magnified. The methanol solution is fed into the AFC and transfers through the ADL into the ACL by convection and diffusion. It can be seen from Fig. 5 that the liquid pressure at $x = 0$, that is the pressure of the methanol solution in the AFC, decreases obviously along the flow direction. This pressure drop results from the friction resistance, gravitation, and accelerated flow due to the appearance of CO_2 gas. For the liquid flow in y-direction, the flow in the AFC dominates the flow in the porous region due to the assumption of neglecting the flow and mass transport in this region. Thus, the liq-

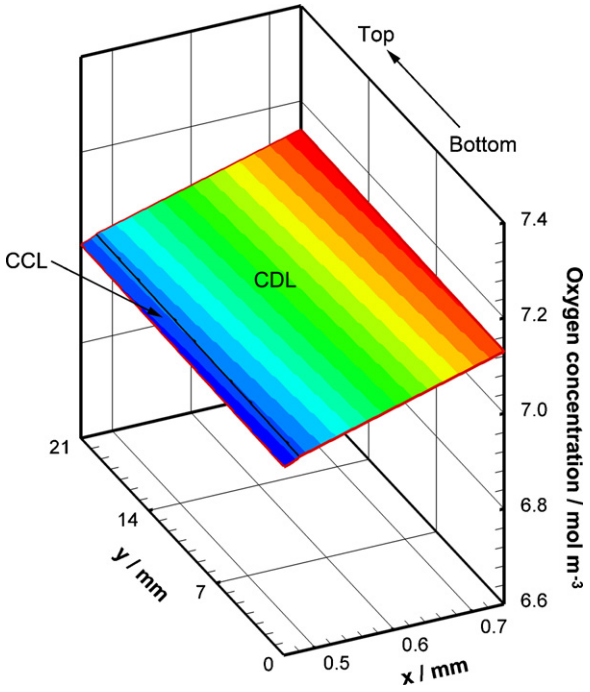

Fig. 4. The distribution of oxygen concentration in the cathode porous region.

uid pressure in the ADL and ACL decreases along the flow direction similar to that in the AFC. However, the liquid pressure along the *x*-direction is almost constant in the ADL, and decreases slightly in the ACL. The slight variation of the liquid pressure in the porous region may be attributed to the positive pressure gradient from the anode to the cathode established in the operation cell which hinders the liquid convection. Hence diffusion is the dominator in the anode porous region resulting in the slight change of the liquid pressure. Following the methanol arriving the catalyst sites, CO_2 gas is produced by the methanol oxidation reaction in the ACL and transfers through the ADL into the AFC by diffusion and convection. The gas pressure, which is determined by the liquid pressure and capillary pressure, cf. Eq. (13), is predicted and shown in Fig. 6. The gas pressure decreases along the *y*-direction and varies significantly and non-linearly across the porous region. The calculation shows the pressure drop is about 700 Pa from the ACL to the ADL. It can be expected that decreasing liquid pressure in *y*-direction dominates the decrease in the gas pressure along the flow direction, while the increased capillary pressure resulted from the decreased liquid saturation (cf. Fig. 8b) determines the non-linear increase in the gas pressure in *x*-direction. It should be noted that the liquid and the gas pressure gradients are different at the interface between the ADL and ACL, though the flow is continuous across the interface. This can be understood from Eqs. (11) and (12) considering different permeabilities (K and k_{rg}) of these two layers. Furthermore, it should be pointed out that the gas pressure is lower than the liquid pressure in the anode porous region because of the negative capillary pressure resulting from its hydrophobicity.

Water is produced in the CCL by oxygen reduction reaction and expelled through the CDL by the capillary pressure in the cathode. Fig. 7 shows the liquid pressure distribution in the cathode porous region. The cathode liquid pressure is constant along the *y*-direction resulting from a constant cathode gas pressure and a constant liquid saturation at the CDL surface facing the atmosphere. However, the calculation shows a significant drop (1449 Pa) in the liquid pressure across the CCL, which is mainly resulted from a very low permeability. Then the liquid pressure decreases linearly through the CDL. Similar to the anode, different liquid pressure gradients appear at the interface between the CDL and CCL due to different permeabilities, and the liquid pressure is also higher than the gas pressure (a constant value of 101300 Pa) resulting from its hydrophobicity.

3.4. Liquid saturation and relative humidity distribution

The predicted liquid saturations in the AFC and in the anode porous region at different locations in the *y*-direction are shown in Fig. 8. It is clear that the liquid saturation in the AFC decreases linearly along the flow direction due to the methanol solution consumption and the produced CO_2 gas accumulation. The liquid saturation in the anode porous layers keeps almost same along the *y*-direction, which is mainly caused by the assumption of neglecting flow and mass transports along the *y*-direction. Furthermore, the liquid saturation decreases slowly from $x = 0$ in the ADL as a result of one-way transport of the methanol solution. Then, the liquid saturation drops dramatically from 0.92 to 0.41 at the interface between the ADL and ACL, and decreases slightly in the ACL due to a rather small capillary pressure gradient (cf. Figs. 5 and 6). The main

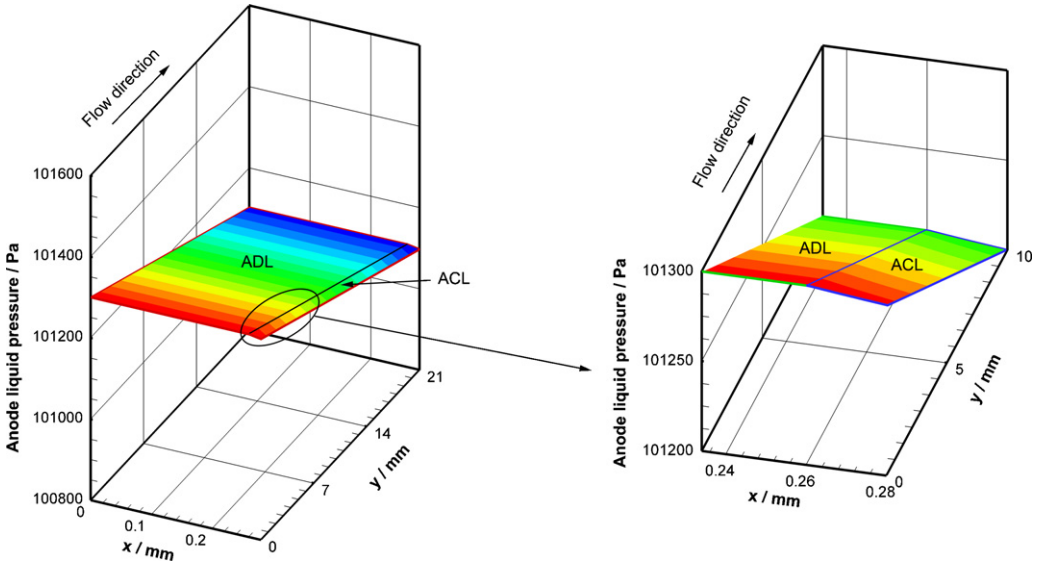

Fig. 5. The distribution of liquid pressure in the anode porous region.

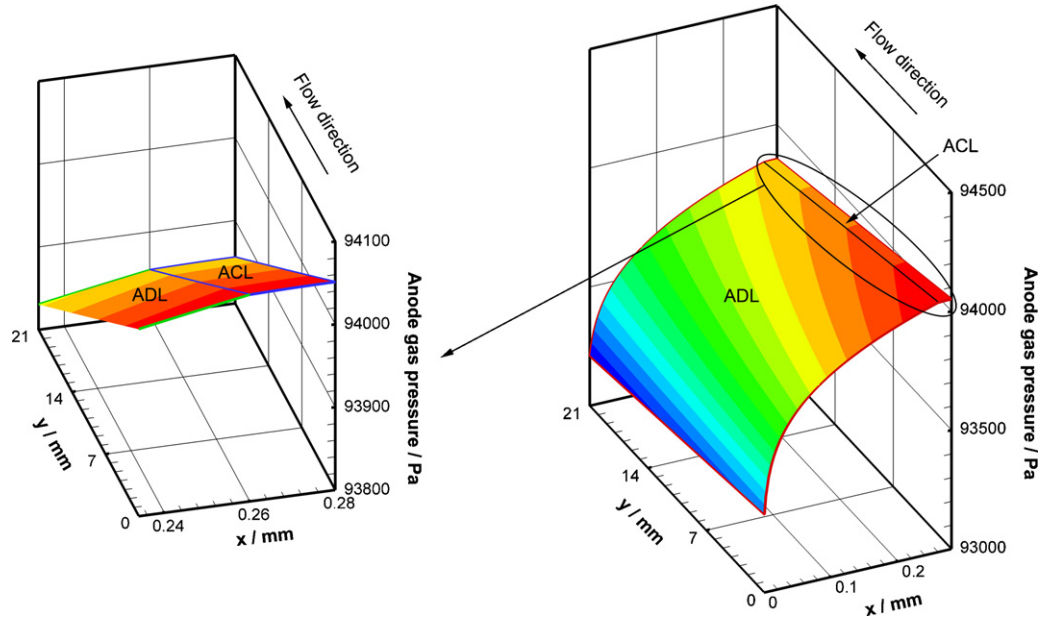

Fig. 6. The distribution of gas pressure in the anode porous region.

cause which results in the significant drop in the liquid saturation at the interface is the different porosity and permeability at these two layers under the continuous capillary pressure, especially the permeability of the ADL being about two orders of magnitude larger than that of the ACL.

Distributions of the liquid saturation in the cathode porous region at different locations in the *y*-direction are shown in Fig. 9a. The cathode liquid saturation almost remains same along the *y*-direction due to the constant liquid pressure, cf. Fig. 7. Accompanying with the process of liquid water transferring from the CCL

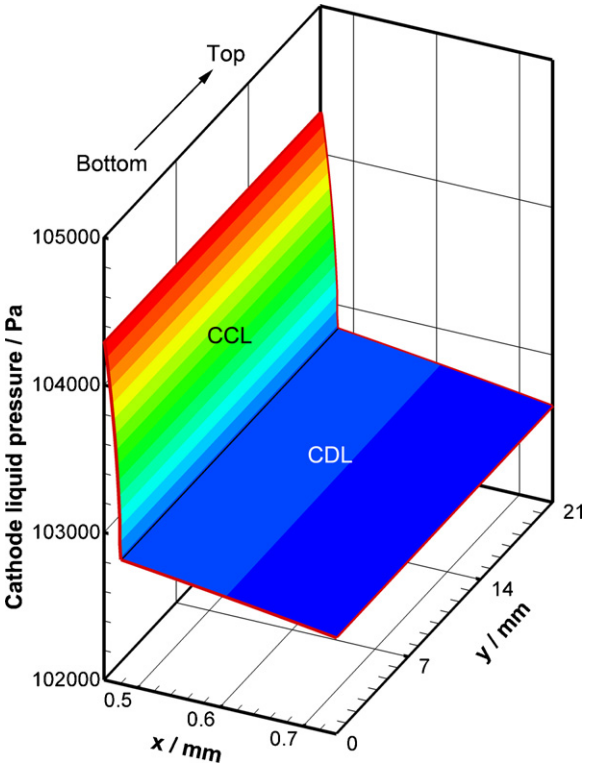

Fig. 7. The distribution of liquid pressure in the cathode porous region.

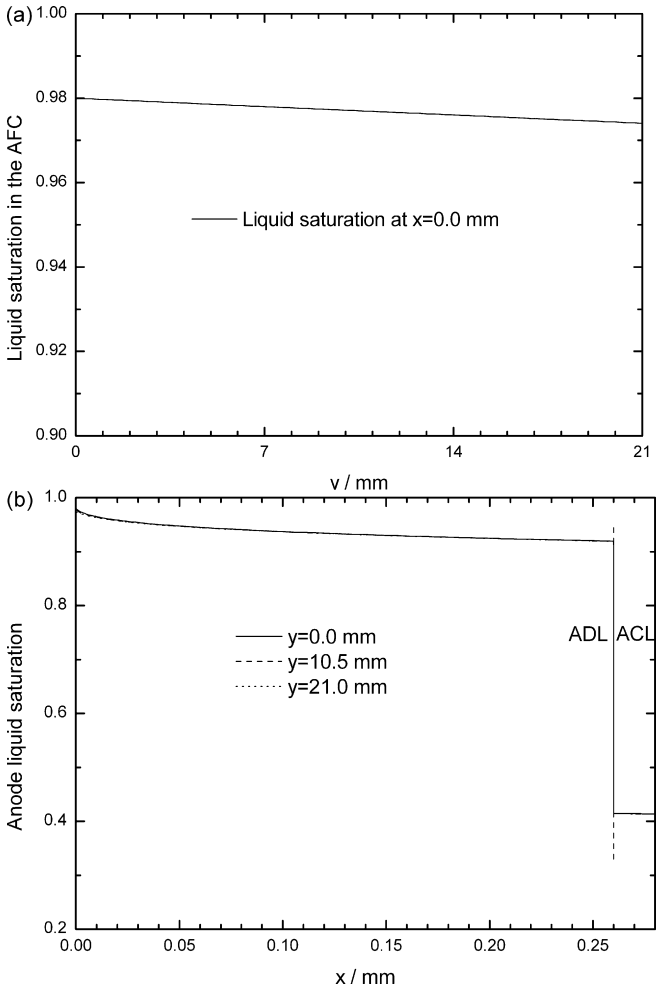

Fig. 8. Distributions of (a) liquid saturation in the AFC and (b) liquid saturation in the anode porous region at different locations in the *y*-direction.

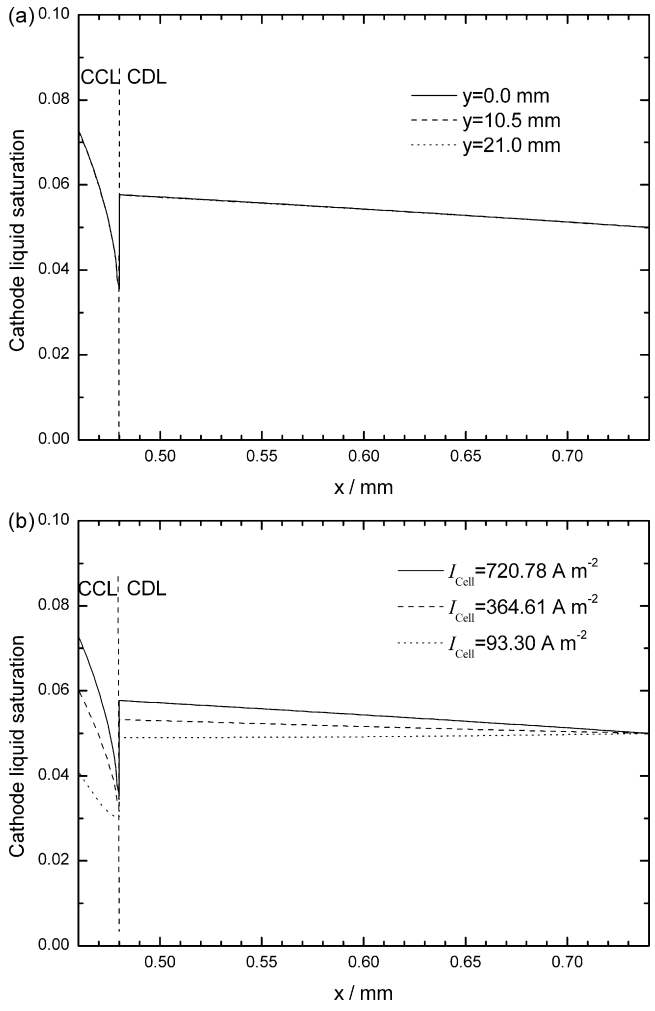

Fig. 9. Distributions of liquid saturation in the cathode porous region: (a) at different locations in the y-direction; (b) at $y = 0.0$ mm for different current densities.

to the outer surface of CDL, the cathode liquid saturation decreases non-linearly across the CCL, then rises from 0.035 to 0.058 at the interface between the CCL and CDL, and finally decreases linearly across the CDL. The jump of the liquid saturation at the interface $x = x_{acl}$ can also be attributed to the continuous capillary pressure but different permeability and porosity at these two layers. Furthermore, the liquid saturation distributions through the cathode at the same location for different current densities are shown in Fig. 9b. With the increase in the current density, the liquid saturation increases in both the CCL and CDL due to the increased water resulting from the oxygen reduction reaction and water crossover from the anode. However, it is noted that the increase in the liquid saturation at the CCL is higher than that at the CDL.

The evaporation of the liquid water is taken into account in the present model. The relative humidity in the cathode porous region can be obtained from the concentration of water vapor coupled with the calculations of current density, oxygen concentration, liquid saturation and pressure. Fig. 10 shows distributions of the relative humidity in the cathode at current densities of 93.30 A m^{-2}, 364.61 A m^{-2}, and 720.78 A m^{-2}, respectively. The relative humidity decreases across the cathode porous region from the CCL to the CDL for all current densities. The relative humidity increases with increasing current density comparing Fig. 10a–c. It can be expected that a large current density leads to a high production rate of the liquid water and a large water crossover flux, hence a high interfacial transfer rate between liquid water and vapor. In addition, the relative humidity along y-direction is almost uniform as the result of the constant liquid saturation in y-direction, which can be easily understood with the help of Fig. 9a.

3.5. Methanol crossover

It is known that methanol crossover will definitely deteriorate the cell performance. As mentioned before, diffusion, electro-osmosis and hydraulic pressure difference determine the methanol crossover flux. Fig. 11 shows the variation in the methanol crossover flux with the current density for various methanol concentrations. For a given current density, the methanol crossover flux increases with increasing methanol concentration. For a given methanol concentration, it increases with increasing current density for the concentrations of 2 M and 4 M, while it increases slightly at low current densities and decreases at high current densities for 1 M. For further understanding the mechanism of the methanol crossover, the total methanol crossover flux and its three contributors at different feed methanol concentrations are predicted by the present model as shown in Fig. 12. It is can be seen that for both 4 M and 1 M feed concentrations, diffusion predominates the methanol crossover at low current densities, while electro-osmosis is the dominator at high current densities. The weakening effect of the diffusion on the methanol crossover flux can be explained by the fact that a high current density leads to a high methanol consumption rate hence a low methanol concentration at the interface between the ACL and MEM for either methanol concentration. However, different enhancing effect of the electro-osmosis on the methanol crossover at various methanol concentrations can be seen from Fig. 12. The methanol crossover flux driven by the electro-osmosis significantly increases with increasing current density at 4 M, while it first increases and then decreases at 1 M. The variation in the methanol crossover flux driven by the electro-osmosis is due to the combined effect of the increased current density and the decreased methanol concentration at the interface $x = x_{acl}$. In addition, the hydraulic pressure difference has a negative effect on the methanol crossover due to higher liquid pressure at the cathode, but the variation of the absolute value in the methanol crossover flux driven by the pressure difference is similar to that by electro-osmosis for both 4 M and 1 M. This result is also attributed to a combined effect of the increased cathode liquid pressure and the decreased methanol concentration at $x = x_{acl}$. It can be concluded that decreased concentration at the interface $x = x_{acl}$ plays a critical role in methanol crossover for low feed methanol concentrations, which leads to the decrease in the methanol crossover flux at high current densities.

Taking account of the methanol crossover, the fuel utilization efficiency in the DMFC can be calculated by:

$$\eta_{fuel} = \frac{I}{I + I_P}. \tag{34}$$

Fig. 13 shows the fuel utilization efficiency for various methanol concentrations. The fuel utilization efficiency increases with increasing current density because of a decreased ratio of the parasitic current density to the current density, even though the methanol crossover flux increases simultaneously at high feed methanol concentrations. In addition, high fuel utilization efficiency at low methanol concentrations is observed due to small methanol crossover flux as discussed before.

3.6. Water crossover

The net water transport coefficient is widely used to describe the water crossover flux through the MEM [42,43]. According to Eq. (18), the net water transport coefficient, α_w, can be obtained by:

$$\alpha_w = N_w^{mem}\frac{F}{I} = n_{d,w} - \frac{F}{I}\frac{\rho_l}{M_w}\frac{K(p_{l,c} - p_{l,a})}{\mu_l \delta_{mem}}, \tag{35}$$

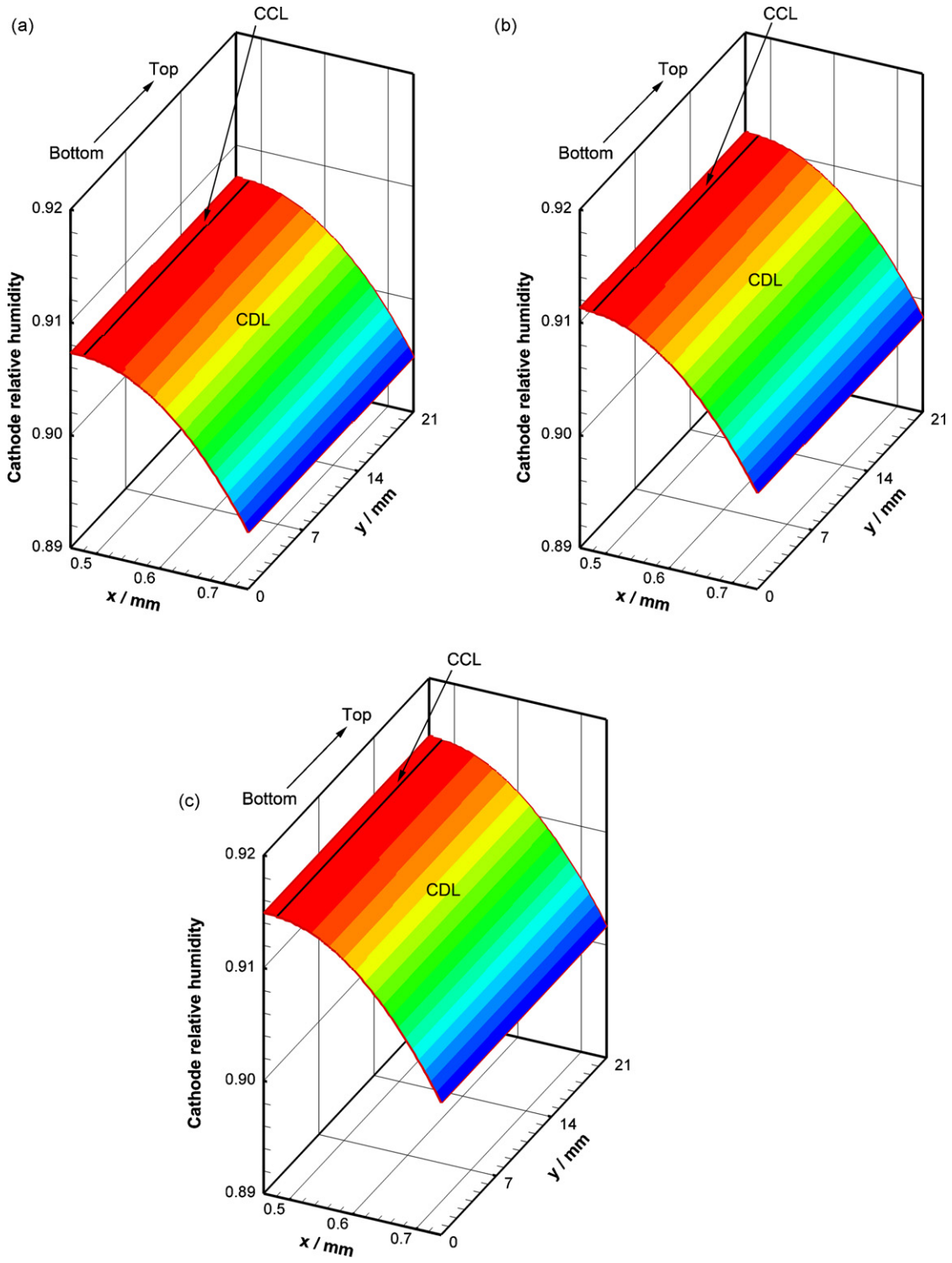

Fig. 10. Distributions of relative humidity in the cathode at different current densities: (a) 93.30 A m^{-2}; (b) 364.61 A m^{-2}; (c) 720.78 A m^{-2}.

The electro-osmotic drag coefficient of water, $n_{d,w}$, is a constant at a given temperature (see Table 4). Thus, the net water transport coefficient depends on the current density and the hydraulic pressure difference across the MEM. A positive α_w represents a net water transport from the anode to the cathode, while a negative α_w denotes a reversed transport. Fig. 14 shows the predicted net water transport coefficient and its contributors for 4 M feed concentration. It is can be seen that the net water transport coefficient increases rapidly at low current densities, and then tends to a mild increase for current densities higher than 200 A m^{-2}. This can be understood by the variation in the water crossover flux driven by electro-osmosis and hydraulic pressure difference. It is clear that the water crossover flux is dominated by the electro-osmosis and the hydraulic pressure difference across the MEM at low current densities, while electro-osmosis plays an essential role at high current densities.

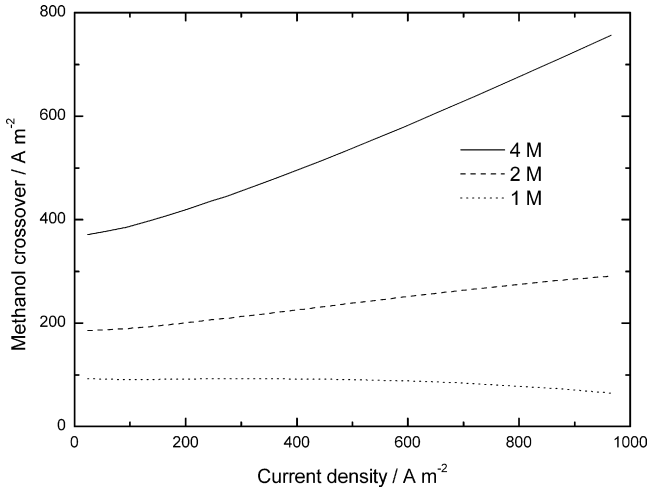

Fig. 11. The variation in the methanol crossover flux with the current density for various methanol concentrations.

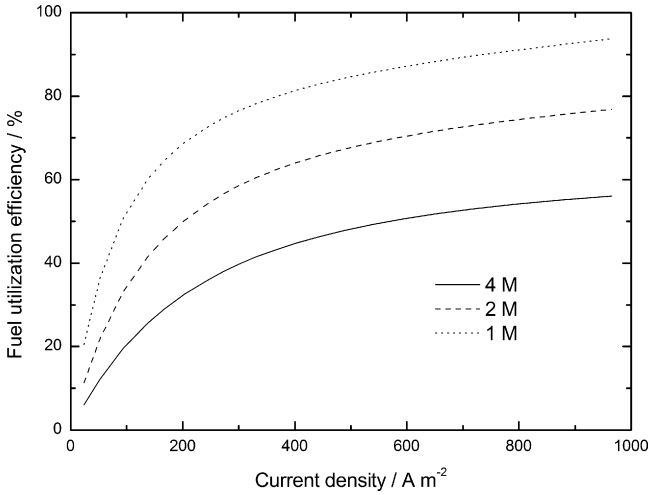

Fig. 13. The fuel utilization efficiency for various methanol concentrations.

In addition to the water crossover flux, the total water flux at the cathode is predicted as follows:

$$N_w^{total} = N_w^{mem} + N_w^{ORR} + N_w^{ORPM}, \quad (36)$$

where N_w^{mem} denotes the water crossover flux from the anode to the cathode, N_w^{ORPM} represents the water flux produced by the ORR in the cathode given by:

$$N_w^{ORR} = \frac{I}{2F}, \quad (37)$$

and N_w^{ORPM} is the water flux generated by the oxidation reaction of permeated methanol (ORPM) calculated from:

$$N_w^{ORPM} = \frac{I_P}{3F}. \quad (38)$$

The variation in the total water flux and its contributors with the current density at 4 M feed concentration is shown in Fig. 15. It is noted that a significant increase in the total water flux is observed with increasing current density, which can be understood from the characters of its three contributors. First, the water crossover flux increases evidently with the increase in the current density as mentioned above. Second, the water flux produced by the ORR is directly proportional to the current density according to Eq. (37). At last, the water flux from the ORPM is in direct proportion to the parasitic current density which increases with increasing current density (cf. Fig. 11). Moreover, it can be concluded from Fig. 15 that the total water flux at the cathode is originated primarily from the water generated by the oxidation reaction of the permeated methanol at low current densities. However, the water crossover flux is the main source of the total water flux at the cathode once the current density is higher than 300 A m^{-2}.

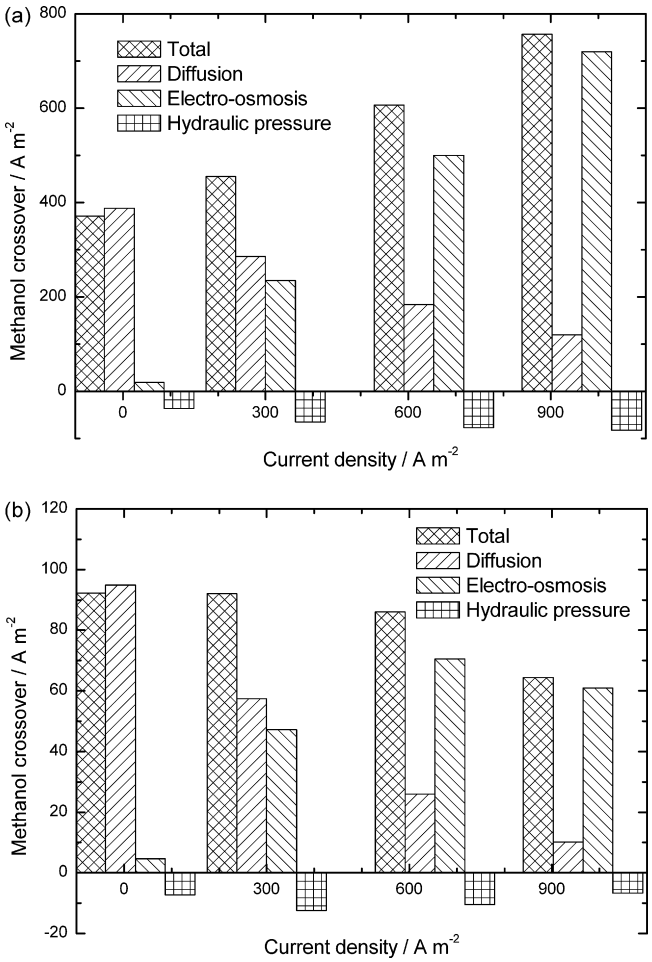

Fig. 12. The total methanol crossover flux and its three contributors at different feed methanol concentrations: (a) 4 M; (b) 1 M.

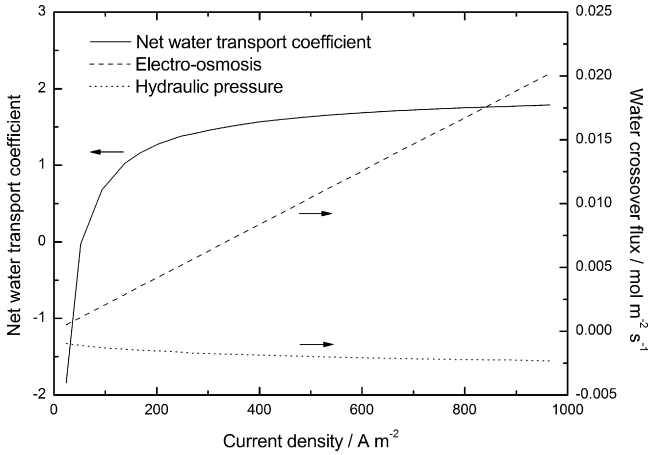

Fig. 14. The net water transport coefficient and its contributors at 4 M feed concentration.

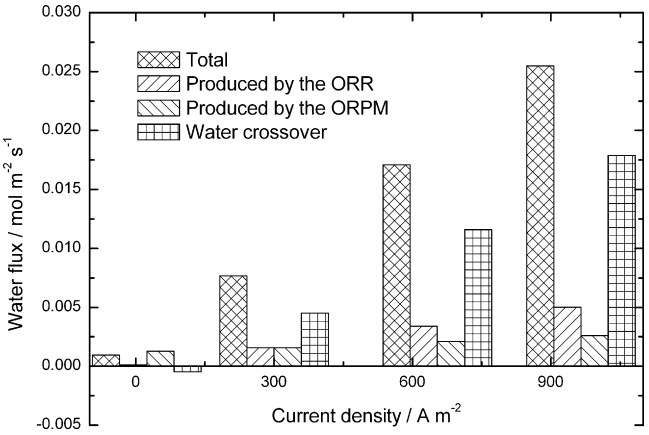

Fig. 15. The variation in the total water flux and its contributors with current density at 4 M feed concentration.

4. Conclusions

A two-dimensional two-phase mass transport model is developed for a vertical air-breathing direct methanol fuel cell, where the discontinuity of liquid saturation at the interface between the diffusion layer and catalyst layer as well as the mass transport in the catalyst layer is considered. The predicted cell performance agrees well with the experimental data within a wide current density range. The typical two-phase flow and mass transport distributions at both the anode and the cathode, the methanol crossover, the net water transport coefficient, the water crossover flux, and the total water flux at the cathode and their contributors are predicted. The main results of the present model are summarized below:

(1) The methanol concentration decreases across the ADL, ACL and MEM and goes down slightly along the flow direction in the AFC, and the oxygen concentration decreases from the CDL to CCL but increases along the flow direction of methanol solution.
(2) The anode gas pressure increases greatly across the ADL, while the cathode liquid pressure drops significantly across the CCL.
(3) The liquid saturation decreases significantly across the ADL and the CCL, and it drops to a smaller value from the diffusion layer to the catalyst layer at both the anode and cathode.
(4) The weakening effect of diffusion and the different enhancing effect of electro-osmosis on the methanol crossover are found for various methanol concentrations. Diffusion dominates the methanol crossover at low current densities, while the electro-osmosis is the dominator at high current densities.
(5) Water transport through the MEM depends on electro-osmosis and hydraulic pressure difference across the MEM at low current densities, while electro-osmosis plays a critical role in the water crossover at high current densities. The total water flux at the cathode is originated primarily from the water generated by the oxidation reaction of the permeated methanol at low current densities, while the water crossover flux is the main source of the total water flux at high current densities.

Acknowledgements

The authors are grateful for the support of National Natural and Science Foundation of China (No. 50876119), NCET-07-0912, and Natural Science Foundation Project of Chongqing (No. CSTC, 2008BB6046).

References

[1] D. Kim, E.A. Cho, S.A. Hong, I.H. Oh, H.Y. Ha, J. Power Sources 130 (2004) 172–177.
[2] B. Bae, B.K. Kho, T.H. Lim, I.H. Oh, S.A. Hong, H.Y. Ha, J. Power Sources 158 (2006) 1256–1261.
[3] W.M. Yang, S.K. Chou, C. Shu, J. Power Sources 164 (2007) 549–554.
[4] J.G. Liu, T.S. Zhao, Z.X. Liang, R. Chen, J. Power Sources 153 (2006) 61–67.
[5] D. Chu, R. Jiang, J. Power Sources 51 (2006) 5829–5835.
[6] R. Chen, T.S. Zhao, J. Power Sources 167 (2007) 455–460.
[7] R. Chen, T.S. Zhao, Electrochim. Acta 52 (2007) 4317–4324.
[8] R. Chen, T.S. Zhao, J.G. Liu, J. Power Sources 157 (2006) 351–357.
[9] Z. Guo, Y. Cao, J. Power Sources 132 (2004) 86–91.
[10] Y. Yang, Y.C. Liang, J. Power Sources 165 (2007) 185–195.
[11] Y.H. Chan, T.S. Zhao, R. Chen, C. Xu, J. Power Sources 176 (2008) 183–190.
[12] R. Chen, T.S. Zhao, Electrochem. Commun. 9 (2007) 718–724.
[13] H.K. Kim, J.M. Oh, J.H. Kim, H. Chang, J. Power Sources 162 (2006) 497–501.
[14] B.K. Kho, B. Bae, M.A. Scibioh, J. Lee, H.Y. Ha, J. Power Sources 142 (2005) 50–55.
[15] A. Blum, T. Duvdevani, M. Philosoph, N. Rudoy, E. Peled, J. Power Sources 117 (2003) 22–25.
[16] K.Y. Song, H.K. Lee, H.T. Kim, Electrochim. Acta 53 (2007) 637–643.
[17] P.W. Li, T. Zhang, Q.M. Wang, L. Schaefer, M.K. Chyu, J. Power Sources 114 (2003) 63–69.
[18] C. Ziegler, A. Schmitz, M. Tranitz, E. Fontes, J.O. Schumacher, J. Electrochem. Soc. 151 (2004) A2028–A2041.
[19] J.J. Hwang, S.D. Wu, L.K. Lai, C.K. Chen, D.Y. Lai, J. Power Sources 161 (2006) 240–249.
[20] J.J. Hwang, S.D. Wu, R.G. Pen, P.Y. Chen, C.H. Chao, J. Power Sources 160 (2006) 18–26.
[21] R. O'Hayre, T. Fabian, S. Lister, F.B. Prinz, J.G. Santiago, J. Power Sources 167 (2007) 118–129.
[22] Y. Zhang, R. Pitchumani, J. Power Sources 50 (2007) 4698–4712.
[23] B.P.M. Rajani, A.K. Kolar, J. Power Sources 164 (2007) 210–221.
[24] Y. Wang, T.H. Yang, W.Y. Lee, J. Ke, C.S. Kim, J. Power Sources 145 (2005) 572–581.
[25] Y. Wang, M. Ouyang, J. Power Sources 164 (2007) 721–729.
[26] S. Lister, N. Djilali, Electrochim. Acta 52 (2007) 3849–3862.
[27] M. Paquin, L.G. Fréchette, J. Power Sources 180 (2008) 440–451.
[28] V. Saarinen, O. Himanen, T. Kallio, G. Sundholm, K. Kontturi, J. Power Sources 172 (2007) 805–815.
[29] R. Chen, T.S. Zhao, J. Power Sources 152 (2005) 122–130.
[30] T.K. Yeh, C.H. Chen, J. Power Sources 175 (2008) 353–362.
[31] R. Chen, T.S. Zhao, W.W. Yang, C. Xu, J. Power Sources 175 (2008) 276–287.
[32] J. Rice, A. Faghri, Int. J. Heat Mass Transfer 49 (2006) 4804–4820.
[33] J. Rice, A. Faghri, J. Heat Transfer 130 (2008) 062001.
[34] B. Xiao, A. Faghri, Int. J. Heat Mass Transfer 51 (2008) 3127–3413.
[35] C. Xu, T.S. Zhao, W.W. Yang, J. Power Sources 178 (2008) 291–308.
[36] U. Pasaogullari, C.Y. Wang, Electrochim. Acta 49 (2004) 4359–4369.
[37] G.Q. Lu, C.Y. Wang, J. Power Sources 134 (2004) 33–40.
[38] H. Yang, T.S. Zhao, Q. Ye, J. Power Sources 139 (2005) 79–90.
[39] Z.H. Wang, C.Y. Wang, J. Electrochem. Soc. 150 (2003) A508–A519.
[40] U. Pasaogullari, C.Y. Wang, J. Electrochem. Soc. 151 (2004) A399–A406.
[41] W.W. Yang, T.S. Zhao, Electrochim. Acta 52 (2007) 6125–6140.
[42] G.Q. Lu, F.Q. Liu, C.Y. Wang, Electrochem. Solid-State Lett. 8 (2005) A1–A4.
[43] F.Q. Liu, G.Q. Lu, C.Y. Wang, J. Electrochem. Soc. 153 (2006) A543–A553.